ARTICLE   OPEN

Check for updates

Multi-scale mechanical properties of bulk-heterojunction films in polymer solar cells

Tian Zhong[1,5], Feng Guo[1,5], Shiyun Lei[1], Biao Xiao [1✉], Qingduan Li[2], Tao Jia[3✉], Xunchang Wang[1] and Renqiang Yang [1,4✉]

The mechanical properties of bulk-heterojunction (BHJ) films play critical roles in the operational stability of flexible polymer solar cells (PSCs). In this study, the multi-scale mechanical properties of the BHJ films containing three representative electron acceptors are systematically evaluated. Interestingly, the tensile moduli of the films based on $PC_{71}BM$, Y6, and PRi-C39 decrease sequentially, and their fracture strain and toughness show an increasing trend. Moreover, the nanoindentation moduli of the films based on these acceptors vary in accordance with the results of tensile characterizations. Creep analyses illustrate that the occurrence of creep deformation in the $PC_{71}BM$, Y6, and PRi-C39-based films decrease sequentially. Contact angle tests demonstrate that the donor-acceptor interactions greatly affect the mechanical properties of these films. All results above demonstrate the effects of acceptor type on the multi-scale mechanical properties of the BHJ films, which are important for the development of reliable flexible PSCs.

INTRODUCTION

In the past decades, the interest from both academia and industry toward flexible polymer solar cells (PSCs) has risen enormously due to their advantages of being conformable, mechanically flexible, and not easily breakable[1–3]. One of the basic requirements for these flexible devices is that the bulk-heterojunction (BHJ) films used as light-harvesting layers must retain flexibility and portability to function in complex deformation conditions. For this consideration, the BHJ films should possess both good optoelectronic and mechanical properties. Over the years, research efforts have been mainly focused on the optoelectronic performance of the BHJ layers[4–7]. However, few attempts have been made to understand the mechanical behaviors of these BHJ layers. In fact, mechanical properties like elasticity, plasticity, and viscoelasticity of the BHJ layers are of critical importance in practical applications since they may affect the long-term stability of flexible devices. The main reason for the lack of mechanical-related research is that the thickness of the BHJ layer is only about 100 nm, and it is difficult to accurately measure the mechanical properties of such thin films experimentally using conventional methods. This situation has been greatly improved after several metrological techniques, including the water-based pull test[8] and nanoindentation[9], were proposed.

The water-based pull test is often referred to as the "film-on-water" (FOW) method, except that the thin film floats on the water surface, this test is very similar to the traditional tensile test. Using the FOW approach, many meticulous studies on the mechanical properties of BHJs were conducted. For example, Kim et al. studied the effect of the ratio of polymer donor to fullerene acceptor on the modulus and toughness of BHJ films, and found that increasing the content of PCBM raises the modulus of BHJ films but decreases their toughness[10]. Ye and co-workers unraveled the

variation of molecular mixing on the mechanical properties of all-polymer BHJs[11]. Wang et al. explored the impact of flexible conjugation-break spacers (FCBS) of non-conjugated polymer acceptors on the mechanical properties of the BHJ layers, and they concluded that introducing appropriate FCBS with short length can simultaneously enhance the photovoltaic performance and mechanical robustness of the devices[12].

Since the FOW method measures the mechanical properties of relatively large-area (usually on the millimeter scale or even larger) films, the local mechanical responses within the films cannot be studied at a more microscopic scale with this method. Nanoindentation is an advanced technique developed for quantitatively probing the mechanical properties of materials at a very small scale (from micron to nanoscale) or at the surface or sub-surface regions[13]. Using this approach, Logothetidis et al. studied the effect of the fullerene presence and the annealing on the P3HT:PCBM nanomechanical behaviors[14]. Jeng and coworkers determined the hardness and modulus of the P3HT:PCBM blend films, and attempted to correlate the mechanical properties to the power conversion efficiency of devices[15]. The above studies have deepened the understanding of the mechanical properties of BHJ thin films. However, considering the complex scenarios in flexible solar cells, there is still a lot of work to be done. For example, previous studies have not considered the change of mechanical properties of the BHJs over time, which is not in line with the real working conditions of flexible PSCs. In addition, the response of the nanoscale BHJ to periodic external forces is also poorly understood. To clarify these issues, it is necessary to study the mechanical properties of the BHJs at multiple scales.

In this work, multi-scale mechanical properties of the BHJ films with three representative acceptors: the classical fullerene derivative $PC_{71}BM$[16], the fused ring non-fullerene electron acceptor Y6[17], and the polymer acceptor PRi-C39[18] are reported.

---

[1]Key Laboratory of Optoelectronic Chemical Materials and Devices (Ministry of Education), Flexible Display Materials and Technology Co–Innovation Centre of Hubei Province, School of Optoelectronic Materials & Technology, Jianghan University, Wuhan 430056, China. [2]School of Chemistry, Guangzhou Key Laboratory of Materials for Energy Conversion and Storage, Guangdong Provincial Engineering Technology Research Center for Materials for Energy Conversion and Storage, South China Normal University, Guangzhou 510006, China. [3]School of Optoelectronic Engineering, Guangdong Polytechnic Normal University, Guangzhou 510665, China. [4]State Key Laboratory of Luminescent Materials and Devices, South China University of Technology, Guangzhou 510640, China. [5]These authors contributed equally: Tian Zhong, Feng Guo. ✉email: biaoxiao@jhun.edu.cn; tjia@gpnu.edu.cn; yangrq@jhun.edu.cn

Specifically, the FOW method was employed to measure the macroscopic tensile properties (tensile modulus, fracture strain, and toughness) of the BHJ films, and nanoindentation was adopted to study the micro-to-nanoscale mechanical characteristics (distribution of modulus and hardness, elastic and plastic deformation under local compressive stress, etc.) of these films. Especially, the time-dependent mechanical issues, such as creep deformation, are the focus of this research effort. In addition, nano-dynamic mechanical tests, which are useful for evaluating the response of the film to periodic external forces with different frequencies, were performed to investigate the effect of the interaction between the electron donor and electron acceptor on the mechanical properties of the films. Finally, the relative strength of the interaction between the donor and the acceptor was studied experimentally by using contact angle measurements. The implications of the results are also discussed for the potential application of flexible PSCs.

RESULTS AND DISCUSSION
Tensile mechanical properties

To explore the mechanical properties of the BHJ films, three typical acceptors, namely the fullerene derivative $PC_{71}BM$, the non-fullerene electron acceptor Y6, and the polymer acceptor PRi-C39, were selected as the research objects. For donor materials, high-efficiency donor polymers PM6[19], PTB7-Th[20], and D18-Cl[21] were chosen (Fig. 1a). Photovoltaic properties of the devices with PM6 as the donor and $PC_{71}BM$, Y6, and PRi-C39 as the acceptors are placed in Supplementary Fig. 1. The FOW technique was firstly employed to investigate the tensile mechanical properties of the BHJ blend films[8,11], and a schematic illustration of the test process is shown in Fig. 1b. Through this test, the intrinsic mechanical properties of the nanofilms, including tensile modulus, fracture strain, and toughness can be directly measured without any approximations or assumptions. Stress-strain curves for PM6, PTB7-Th, and D18-Cl-based photoactive layers with different acceptors are presented in Fig. 1c–e, respectively. Regardless of the donor material used, when $PC_{71}BM$ and Y6 were employed as acceptors, the stress of the blend film increased substantially and linearly with increasing strain until the films break. However, the all-polymer films based on PRi-C39 displayed distinct characteristics. As the strain increased, the stress-strain curves firstly rose linearly, and when the strain reached a certain critical value, the growth rate of the curves slowed down. With a further increase in strain, the stress of the film slowly decreased, and eventually the fracture occurred. In addition, the slopes of the curves based on $PC_{71}BM$, Y6, and PRi-C39 films decreased sequentially in the linear growth stage, indicating that their tensile moduli decrease accordingly. Table 1 summarizes the statistical results of the thin film mechanical parameters extracted from the stress-strain curves. Taking PM6-based BHJ films as an example, the average values of tensile modulus were measured to be 1.22 ± 0.20, 0.61 ± 0.19, and 0.33 ± 0.04 GPa when $PC_{71}BM$, Y6, and PRi-C39 were selected as the acceptors, respectively, indicating that the rigidity of the active layer film can be adjusted in a wide range by using different kinds of acceptors. Specifically, the films with $PC_{71}BM$ as the acceptor had the highest rigidity, followed by the Y6 films, and the PRi-C39 films with the lowest rigidity.

In addition, the fracture strain values (the ratios between the changed lengths at fracture and the initial lengths) of these films were also significantly different. The fracture strains of $PC_{71}BM$ films were generally small, ranging from 1.7% to 2.7%, indicating that these films are very brittle. After replacing $PC_{71}BM$ with small molecule Y6, the brittleness of the films was reduced to a certain extent, and their fracture strains were improved to be 3.0–5.5%. Surprisingly, the fracture strain of PRi-C39-based films was generally above 20%, and the average value of PM6:PRi-C39 film

was even as high as 35.1%. It is worth noting that such high fracture strains in the all-polymer systems can meet the requirements (tensile strain over 20%) needed for the applications in the field of wearable electronics[22,23]. In other words, the small fracture strains of $PC_{71}BM$- and Y6-based films will limit their applications in flexible devices. Figure 1f illustrates the pre-tensile and fracture scenarios in these films. For the fullerene systems, due to the large surface energy difference between the $PC_{71}BM$ aggregates and the polymer donors (which will be discussed later), the films are prone to crack along the interfaces between the donors and the acceptors under external stress[24], which results in low fracture strains. In the all-polymer films, the molecular chains of the donors and acceptors are in a state of entanglement, and the external stress is not easy to cause a large unrecoverable relative displacement of the molecular chains, this is the reason why the all-polymer systems have the highest fracture strains. For the Y6 based films, on the one hand, since the surface energy difference between Y6 and the donor is smaller than that between $PC_{71}BM$ and the donor, the interaction between Y6 and the donor is stronger. On the other hand, as the chain length of the Y6 molecule is shorter than that of PRi-C39, the degree of entanglement between Y6 and the donors is lower. Therefore, the fracture characteristics of the Y6 systems are between the $PC_{71}BM$ and PRi-C39 systems.

The mechanical properties of the blend films were also checked by comparison of the toughness. A remarkable contrast in the toughness values of the all-polymer films with the $PC_{71}BM$ and Y6 films was observed. For the PM6 systems, the toughness of the PRi-C39 films (5.44 ± 0.87 MJ m^{-3}) was ~16 times greater than that of the $PC_{71}BM$ films (0.34 ± 0.10 MJ m^{-3}) and ~6–fold higher compared to that of the Y6 thin films (0.90 ± 0.18 MJ m^{-3}). It should be noted that similar results also appeared in the PTB7-Th and D18-Cl systems. Since the toughness is indicative of a material's resistance to fracture, it is believed that the all-polymer films have very good ability to absorb energy and plastically deform without fracturing when a crack is present.

Creep deformation is a time-dependent mechanical issue often encountered when polymer-based materials are used[25–27], it refers to the phenomenon that the deformation of a material increases with time under constant stress. The reliability of the flexible PSCs may be affected by the creep deformation during devices being on service under long-term stress conditions. To the best of our knowledge, no previous studies have been conducted on the creep properties of active layer thin films in PSCs. In this context, we performed an in-depth study on the creep properties of PM6-based active layers using the FOW method. The creep curves of the PM6-based blend films with different acceptors are presented in Fig. 2a. In all creep curves, an instantaneous increase in strain occurred and was followed by a time-dependent rise. Within the test range, the strain values of the all-polymer film were always the largest, indicating that its creep is the most obvious. In contrast, under the same condition, the strain and its time dependence of PM6:Y6 films were moderate. Unlike the PRi-C39 and Y6 films, the creep curve of the fullerene film was very stable, and the strain values were always the smallest. These results suggest that the all-polymer system is prone to creeping under constant external force, while the fullerene film has a better creep resistance.

To understand how the acceptor affects the creep behavior of the film, a four-element viscoelastic model (Fig. 2b) was employed to analyze the creep deformation of the BHJ films[28]. In this model, the total strain ε is composed of three independent components ε_1, ε_2, and ε_3. The ε_1 is the general elastic deformation caused by the change of bond length and bond angle inside the molecule. When the material is subjected to external force, the bond length and bond angle in its molecular chain will change immediately. Since the chemical bond is rigid, this deformation has the characteristics of ideal elasticity, and is completed instantaneously
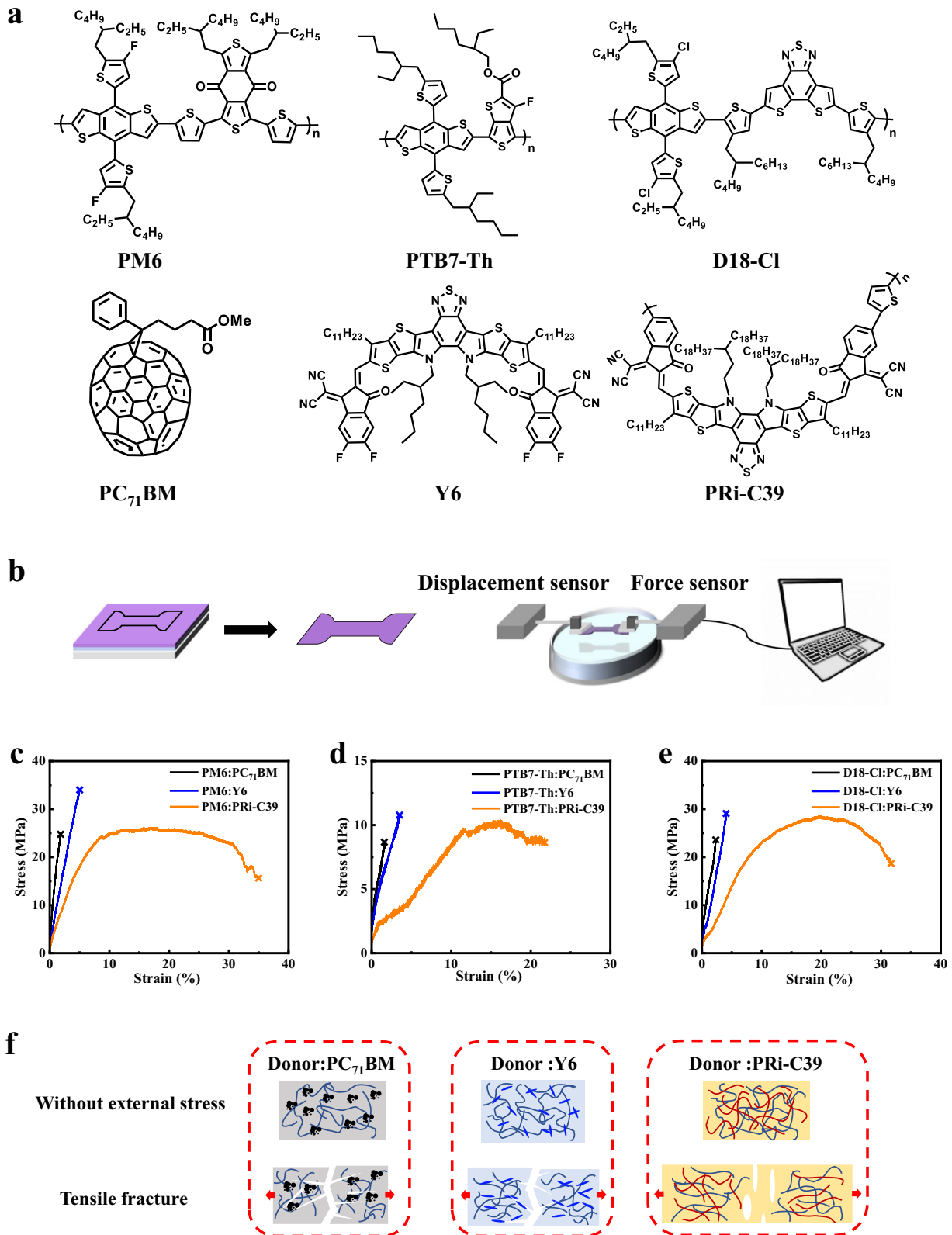
Fig. 1 Tensile testing of BHJ films based on different electron acceptor materials. a Molecular structures of the photovoltaic materials used in the study. **b** Schematic illustration of the tensile test of films on water. The film is firstly spin-coated on the substrate, then etched into a dog-bone shape by laser etching, and finally, a high-precision force sensor and a linear displacement stage are used for data acquisition. The stress-strain curves of **c** PM6, **d** PTB7-Th, and **e** D18-Cl-based blend layers. **f** Schematic diagram of the films under no stress and fracture.

Table 1. Summary of the mechanical parameters from the stress-strain characterizations.

Donor	Acceptor	Modulus[a] (GPa)	Fracture strain[b] (%)	Toughness[c] (MJ m^{-3})
PM6	PC$_{71}$BM	1.22 ± 0.20	2.7 ± 0.8	0.34 ± 0.10
	Y6	0.61 ± 0.19	5.5 ± 0.9	0.90 ± 0.18
	PRi-C39	0.33 ± 0.04	35.1 ± 6.9	5.44 ± 0.87
PTB7-Th	PC$_{71}$BM	0.44 ± 0.07	1.7 ± 0.1	0.09 ± 0.03
	Y6	0.21 ± 0.06	3.0 ± 0.4	0.13 ± 0.06
	PRi-C39	0.10 ± 0.02	24.3 ± 6.3	1.85 ± 0.51
D18-Cl	PC$_{71}$BM	1.06 ± 0.20	2.0 ± 0.2	0.28 ± 0.02
	Y6	0.83 ± 0.11	4.6 ± 0.8	0.59 ± 0.09
	PRi-C39	0.24 ± 0.01	33.9 ± 7.1	6.73 ± 1.24

[a]Derived from the linear regime of the stress-strain curves using the Hooke's law.
[b]Obtained from the stress at failure.
[c]Calculated by integrating the area under the stress-strain curve.

when the external force is applied. Therefore, this deformation can be calculated using Hooke's law (Eq. 1):

$$\varepsilon_1 = \frac{\sigma}{E_1} \tag{1}$$

where σ is the stress applied to the specimen and E_1 is the coefficient of elasticity of the spring 1. As the polymer chain is usually in a coiled state, hence, its molecular chain gradually stretches upon external force, resulting in the generation of high elastic deformation ε_2. Theoretically, the ε_2 can be described by a parallel combination of an ideal spring (spring 2) and an ideal dashpot (dashpot 2) and expressed by Eqs. 2 and 3 as follows:

$$\varepsilon_2 = \frac{\sigma}{E_2}\left(1 - e^{-\frac{t}{\tau}}\right) \tag{2}$$

$$\tau = \frac{\eta_2}{E_2} \tag{3}$$

where E_2 and η_2 are the coefficient of elasticity of the spring 2 and the coefficient of viscosity of the dashpot 2. In the absence of chemical crosslinking of the molecular chains of the polymer, a relative slippage between the polymer chains will also occur during the creep process, that is, viscous flow. This deformation cannot be recovered after the external force is removed, and thus, it is an irreversible deformation, which is represented by ε_3. The ε_3 can be described by an ideal dashpot (dashpot 1) and expressed by Eq. 4 as follows:

$$\varepsilon_3 = \frac{\sigma}{\eta_1}t \tag{4}$$

where η_1 is the coefficient of viscosity of the dashpot 1. Therefore, the total creep deformation ε is the sum of the above three parts, namely:

$$\varepsilon = \varepsilon_1 + \varepsilon_2 + \varepsilon_3 = \frac{\sigma}{E_1} + \frac{\sigma}{E_2}\left(1 - e^{-\frac{t}{\tau}}\right) + \frac{\sigma}{\eta_1}t \tag{5}$$

The experimentally obtained creep curves were fitted by using Eq. 5, the fitting results are displayed as the solid lines in Fig. 2a, and the parameters used for fitting are summarized in Supplementary Table 1. As a result, the experimental data could be well described by using this theoretical model, indicating the high accuracy of this model. Figure 2c–e presents the relationships of ε_1, ε_2, and ε_3 with creep time, respectively, and the insets describe the schematic diagrams of the creep deformations at the molecular level. As seen in Fig. 2c, the general elastic deformation occurred instantaneously at the moment the external strain was

applied, and thereafter, the values of ε_1 remained unchanged. However, as the high elastic deformation and viscous flow deformation continued to occur, the proportion of ε_1 in the total creep ($\varepsilon_1/\varepsilon$) gradually decreased. After 600 s of creep, the proportion of ε_1 in the total ε of the PC$_{71}$BM, Y6 and PRi-C39 films decreased from the initial 100% to 82.9%, 77.1%, and 58.5%, respectively. Such high proportions indicate that in all these films the creep is dominated by the general elastic deformation throughout the test time range. In addition, the values of $\varepsilon_1/\varepsilon$ in the PC$_{71}$BM-based film were always the largest at each specific time, indicating that the general elastic deformation in the PC$_{71}$BM film is more obvious than that in the Y6 and PRi-C39 films. The variation trend of ε_2 with time was obviously different from ε_1. As shown in Fig. 2d, in the initial stage, ε_2 rose rapidly, then the growth rate gradually slowed down until ε_2 was no longer increasing. Finally, the values of $\varepsilon_2/\varepsilon$ in PC$_{71}$BM, Y6, and PRi-C39 films were ~15.6%, 19.5% and 28.2% at the creep time of 600 s, respectively. As mentioned earlier, ε_3 is an irreversible deformation caused by mutual slippage between polymers, and increases linearly with creep time. As depicted in Fig. 2e, the experimental results were constant with the theoretical model as all the ε_3 rose linearly. Moreover, at the same creep time, the PC$_{71}$BM-based films had the smallest $\varepsilon_3/\varepsilon$ (1.5% at 600 s), indicating that PC$_{71}$BM can effectively "lock" the blend networks. Comparatively, the $\varepsilon_3/\varepsilon$ value of the Y6 film was 3.4%, while that of PRi-C39 was as high as 13.3%. We speculate that in the all-polymer film, both the donor and the acceptor will undergo irreversible intermolecular slip under external force, resulting in much higher $\varepsilon_3/\varepsilon$ values than those in the other two films. The schematic diagram of creep deformation of the films based on different acceptors is shown in Fig. 2f.

Nanoindentation test

The above analyses are based on the macroscale uniaxial tensile tests. However, considering the complexity of the donor: acceptor blend, this experimental approach alone cannot fully reveal the mechanical properties of the films. To further study the mechanical properties of the photoactive layers, the nanoindentation test, an advanced technology that can provide quantitative results at a more microscopic level, was employed to characterize the corresponding films. The schematic diagram of the nanoindentation test together with a typical load versus displacement ($P - h$) curve are exhibited in Fig. 3a. A typical nanoindentation experiment involves applying a load to force an indenter into the sample surface ($A - B$), then holding the load over a period ($B - C$), and finally unloading the force ($C - D$). In a specific study, the force loading, holding, and unloading processes should be set reasonably according to the research purpose. By analyzing the loading/holding/unloading curves, many important mechanical parameters of the film, such as indentation modulus, elastic deformation (h_e), plastic deformation (h_p), and creep depth (h_c) can be accurately determined[29]. To ensure the reliability of the results, 50 sets of nanoindentation experiments were performed on each BHJ film on an area of 5 μm × 5 μm. The representative $P - h$ curves and the modulus distributions of BHJ films based on different electron acceptors are displayed in Figs. 3b and 3c–e, respectively. It is seen that the indentation responses of the three acceptors-based films were highly misaligned, indicating their microscopic mechanical properties are quite different. Figure 3c–e shows that the average indentation moduli of the films based on PC$_{71}$BM, Y6 and PRi-C39 decreased sequentially, which were 13.43, 6.59 and 3.51 GPa, respectively. This trend is the same as that of the tensile elastic modulus results, which verifies the FOW tensile test. Nonetheless, it should be noted that the moduli measured by nanoindentation were generally about an order of magnitude higher than those obtained by the FOW method. There are two possible reasons for this discrepancy: first, the tensile measurement
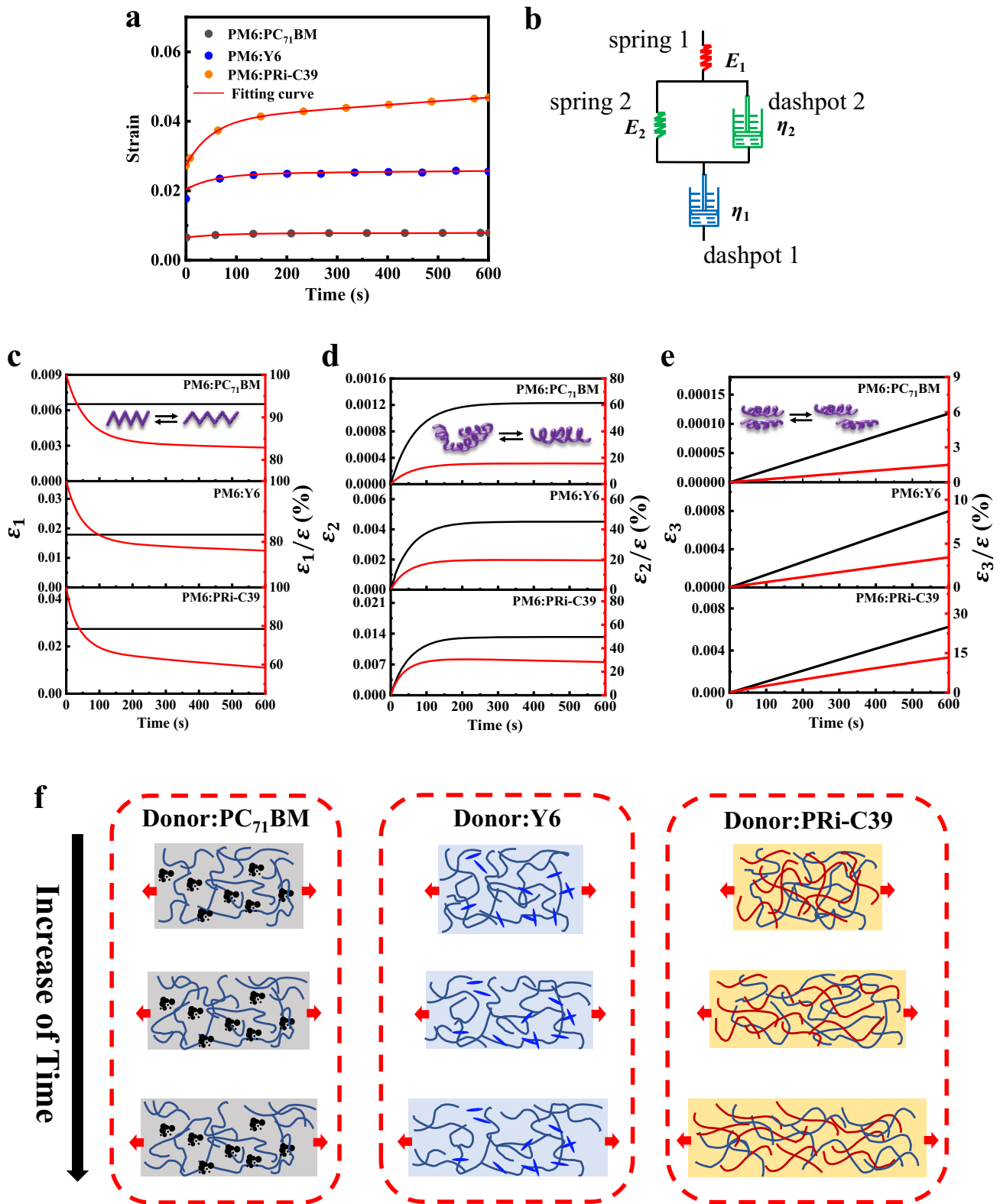
Fig. 2 Creep Behaviors of the BHJ Films. a Creep curves of the PM6-based blend films with different acceptors under the same constant force. b Four-element viscoelastic model used to fit the creep deformation. c ε_1, d ε_2 and e ε_3 and their proportions in the total creep deformations versus creep time. Insets in c–e: Schematic diagram of the molecular movements. f Schematic diagram of creep deformation of the films based on different acceptors.
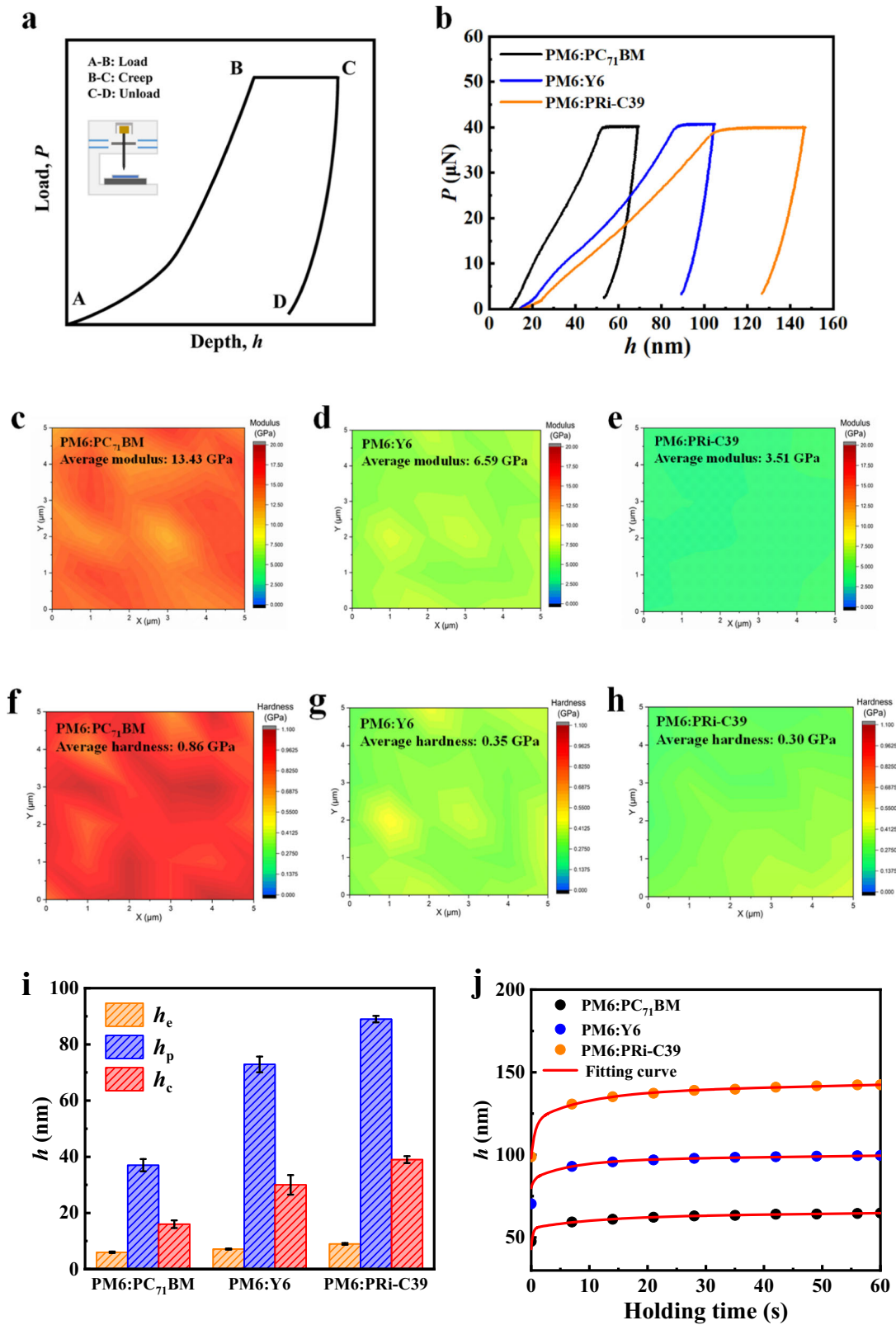
Fig. 3 Nanoindentation test results of the BHJ films. a The schematic diagram of the nanoindentation test together with a typical load versus displacement $(P - h)$ curve. **b** The representative $P - h$ curves of active layer films based on different electron acceptors. The modulus distributions of **c** PM6:PC$_{71}$BM, **d** PM6:Y6, and **e** PM6:PRi-C39 films. The hardness distributions of **f** PM6:PC$_{71}$BM, **g** PM6:Y6, and **h** PM6:PRi-C39 films. **i** The extracted statistical values of h_e, h_p, and h_c from the $P - h$ curves. Data are presented as mean ± SD. **j** Changes of indentation displacement with time during holding.

measures the mechanical properties of the film as a whole, while the results obtained by the nanoindentation measurement are only related to the molecules near the indenter probe; second, when the nanoindentation test is performed, the tested material is in a compressed state, which is obviously different from the tensile test, possibly causing the difference between the two measurement results as well. In fact, relatively high modulus values for conjugated polymer-based films measured by nanoindentation have been reported in previous literature[15,30].

Figure 3f–h depicts, respectively, the maps of the hardness of the PC$_{71}$BM, Y6, and PRi-C39-based photoactive layers in the same area as those of the modulus images. The indentation hardness (H) can be calculated using Eq. 6 as follows[31]:

$$H = \frac{P_{max}}{A_c} \tag{6}$$

where P_{max} is the peak indentation load, and A_c is the projected contact area, which is readily calculated from the contact depth (h_c) using $A_c = 24.5 h_c^2$. As a result, the BHJ appeared uniform in all the three blend films, and this indicates that the acceptors are mixed very uniformly with the polymer donor at the microscopic level, which is also demonstrated by the atomic force microscope test results shown in Supplementary Fig. 2. Moreover, in the tested area, the PC$_{71}$BM-based BHJ film had the largest average hardness with a value of 0.86 GPa, followed by the Y6 film with a hardness lower than half of the former (0.35 GPa). In contrast, the average hardness in the all-polymer BHJ film (0.30 GPa) was slightly lower than that of the Y6 film. According to Eq. 6, since the peak indentation load applied to measure the hardness was the same (40 µN), the reason for the difference in the hardness of these films is that the values of h_c are different, that is, the films deformed differently when subjected to an external load. Therefore, the deformation in the films needs to be further investigated. The extracted statistical values of h_e, h_p, and h_c from the $P - h$ curves are depicted in Fig. 3i, and the corresponding data are shown in Supplementary Table 2. The average h_e for PM6:PC$_{71}$BM, PM6:Y6, and PM6:PRi-C39 BHJ films were measured to be 6.02, 7.13, and 9.04 nm, respectively. It is seen that the h_e in the all-polymer film was much larger than those in the PC$_{71}$BM and the Y6-based films, which is consistent with the variation tendency of the general elastic deformation in the tensile creep test. Due to the use of a sharp indenter tip, large values of h_p were observed in all films. Specifically, the h_p values of PC$_{71}$BM, Y6, and PRi-C39 films were 37.13, 72.88, and 89.11 nm, respectively. Since the h_p of the PC$_{71}$BM film in the indentation experiment was much lower than those of the Y6 and PRi-C39 films, we can reasonably infer that the fullerene electron acceptor can prevent the movement of the donor molecules at the microscopic scale. In fact, this speculation can be further supported by the nanoindentation creep results as the PC$_{71}$BM, Y6 and PRi-C39-based films underwent creep with depths of 16.01, 30.10 and 39.05 nm within the same time period of load holding, respectively. To facilitate comparison, the relative contribution of each component (elastic, plastic, and creep) to the depth of the indentation is presented in Supplementary Fig. 3. Figure 3j shows the changes in indentation displacement with time during holding (nanoindentation creep) at the maximum indentation load for the BHJ films. It is clear that the indentation depth curves can be divided into two regions, i.e., a primary stage and a steady state stage. In the primary stage, the indentation depth increased with holding time, but the rate of ascent decreased gradually. In the second stage, the indentation displacement changed little and remained basically stable. It should be noted that although the displacement-hold time curves shown in Fig. 3j are similar to the strain-time curves shown in Fig. 2a, the two should not be confused because their physical meanings are quite different. During the tensile creep tests, the large-sized films are subjected to the uniaxial tensile stress and the results reflect the behavior of a large number of molecules under

stretching. However, indentation creep is under a localized stress field, and only molecules near the tip of the indenter are involved in the creep process. In addition, the variations of indentation displacement with holding time can be well fitted by the method proposed by Zeng et al. through Eq. 7[32].

$$h = h_0 + h_1[1 - \exp(-t/\tau_1)] + h_2[1 - \exp(-t/\tau_2)] + mt \tag{7}$$

where h_0 is the indentation displacement at the beginning of the creep, ($h_1 + h_2$) describes the limit of the primary creep at a long enough time, τ_1 characterizes the initial creep rate, τ_2 describes the transition from the primary stage to the steady state stage, and m is the steady-state creep rate which is related to the viscosity of the materials. The solid lines in Fig. 3j are the fitting results obtained according to Eq. 7 and the fitting parameters are summarized in Supplementary Table 3. The τ_1 showed an increasing trend in the PM6:PC$_{71}$BM, PM6:Y6 and PM6: PRi-C39 films, with values of 0.26, 0.50, and 0.66 s, respectively, illustrating that the creep in the PC$_{71}$BM film occurs very slowly at the primary stage and the PRi-C39 film creeps much faster after force loading. Moreover, the steady-state creep rate m in the PRi-C39 film was the largest (0.079 nm s^{-1}), followed by the Y6 film (0.045 nm s^{-1}), and the smallest appeared in the PC$_{71}$BM film (0.035 nm s^{-1}). These results show that even when a relatively stable steady state stage is reached, the creep rate of the all-polymer film is still the fastest.

Dynamic mechanical properties

Considering that organic solar cells, especially flexible organic solar cells, may encounter dynamic loads during practical use, it is necessary to study the mechanical properties of the photoactive layers at various strain rates. Typically, storage modulus and loss tangent (tanδ) are parameters often used to describe the dynamic mechanical properties of materials. Since these parameters are sensitive to different kinds of molecular motions, relaxation processes, transitions, and other structural heterogeneities[33], interpreting the parameters could provide information at the molecular level to understand the mechanical behavior of the photoactive layers. Limited by the thickness of the active layers (usually around 100 nm), traditional experimental methods cannot be effectively used to determine the dynamic mechanical properties of the photoactive layers. Herein, the nano-dynamic mechanical analyzer (nano-DMA) technique was employed to study the dynamic mechanical behaviors of these films. In this method, a small periodic load is applied to the nanoscale indentation tip during the loading cycle and by monitoring the phase lag in the load-displacement curve, the frequency-dependent mechanical properties of the material can be evaluated. This technique has been successfully applied in measuring the dynamic mechanical properties of many polymer composites[34–36]. Figure 4 illustrates the behavior of storage modulus and tanδ as a function of loading frequency for various blend films. It is seen from Fig. 4a that the storage moduli of all tested samples remained stable over the test frequency range. Since the storage modulus is a measure of the elasticity of materials, this observation indicates that films based on these three acceptors are capable of withstanding alternating stresses over a wide frequency range. Unlike the storage modulus, the tanδ showed an increasing trend with growing frequency in all films (Fig. 4b). The reason for this growth trend is not clear, we speculate that it may be attributed to an increase in internal friction between the acceptors and PM6 polymer matrix during dynamic loading, which can be understood as follows: as the loading frequency increases, more energy will be dissipated on the donor-acceptor interpenetrating networks near the tip of the indenter, which enhances chain mobility and consequently results in additional viscous response. In fact, the phenomenon that internal friction-induced tanδ increases with frequency has been
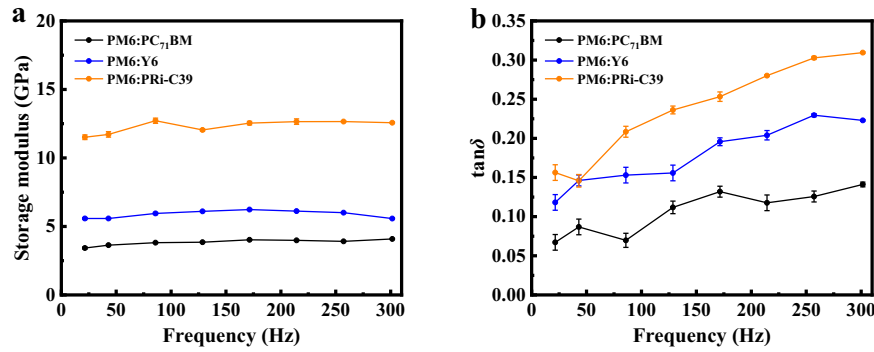
Fig. 4 Nano-DMA test results of the BHJ films. The behavior of **a** storage modulus and **b** tanδ as a function of loading frequency for various blend films. Data are presented as mean ± SD.

reported in other polymer composites[37]. In addition, as seen in Fig. 4b, all the loss tangent values in the test range were <1, indicating that the storage modulus is larger than the loss modulus (shown in Supplementary Fig. 4), which confirms that the mechanical properties of these films are dominated by elasticity rather than plasticity. Moreover, this result is consistent with the small $\varepsilon_3/\varepsilon$ values in the tensile creep experiment (Fig. 2e), which proves the correctness of the tensile creep fitting model (Eq. 5).

Another striking feature in Fig. 4a, b is that the type of electron acceptor had a significant effect on the storage modulus and tanδ of the blend films, and this is another direct evidence that the mechanical properties of the blend films are closely related to the acceptors. Taking the storage modulus as an example, the average storage modulus of the PC$_{71}$BM-based blend film was 12.06 GPa in the test range, while those of the Y6 and PRi-C39 films were 5.78 and 3.69 GPa, respectively. This variation trend was the same as that of the elastic modulus obtained from the previous FOW tensile test.

Donor-acceptor interactions

To experimentally verify that the difference in the interaction between the donor and the acceptor is the reason for the variation in the mechanical properties of the active layer films, the contact angle measurement, by which the Flory-Huggins interaction parameter χ can be calculated from the surface energy γ[38], was conducted. The images of the droplet contact angles (θ) of water and hexadecane on the pure films of PM6, PC$_{71}$BM, Y6, and PRi-C39 are shown in Fig. 5a, and the γ and χ are depicted in Fig. 5b. The values of γ for the PM6, PC$_{71}$BM, Y6, and PRi-C39 pure films were 26.4, 28.7, 27.7, and 27.2 mJ m^{-2}, respectively. Accordingly, the PM6:PC$_{71}$BM, PM6:Y6, and PM6:PRi-C39 pairs exhibited χ values of 4.80×10^{-2} K, 1.56×10^{-2} K, and 5.97×10^{-3} K, respectively. The highest χ value for the PM6:PC$_{71}$BM film indicates weak PC$_{71}$BM − PM6 interactions, and this weak donor-acceptor interaction makes the film easy to crack when subjected to external force, which is the essential reason for the low fracture strain of PM6:PC$_{71}$BM film. While the lower χ value of the PM6:Y6 indicates relatively stronger interactions between the small molecule Y6 and PM6, thus leading to moderate fracture strain. When the polymer PRi-C39 was used as the electron acceptor, the interaction between PRi-C39 and PM6 was the strongest, and cracks are not easy to occur. This reduces the stiffness of the blend film, but also means that the all-polymer film possesses better stretchability.

In conclusion, the multi-scale mechanical properties of three representative electron acceptors-based BHJ films were studied. The tensile modulus of films based on PC$_{71}$BM, Y6, and PRi-C39 measured by using the FOW method decreased sequentially, but their fracture strain and toughness showed an increasing trend. The nanoindentation test results indicated that the modulus and
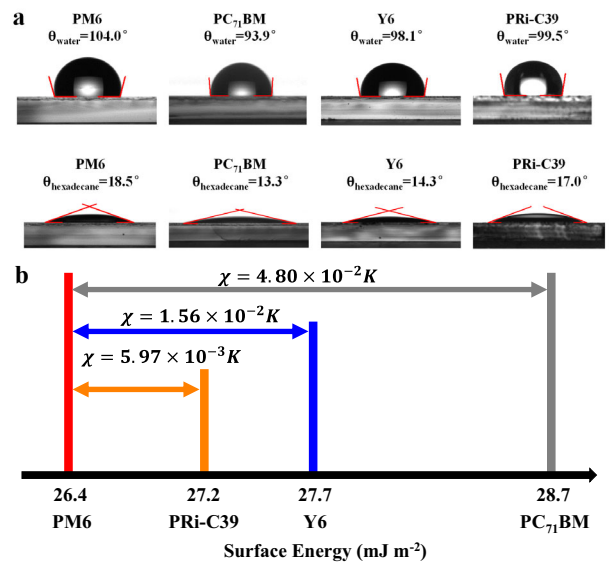

Fig. 5 Interactions between PM6 and the acceptors. a Droplet contact angle images of the pure films of PM6, PC$_{71}$BM, Y6, and PRi-C39. **b** Illustration of calculated surface energy γ and Flory-Huggins interaction parameter χ from the contact angle measurements.

hardness in all of the three different acceptors-based films were uniformly distributed on the nanometer scale. Furthermore, the fullerene acceptor system had the largest average modulus and hardness, while the all-polymer system exhibited the best flexibility. The mechanical properties of small-molecule acceptor-contained films were intermediate between the fullerene systems and the polymer acceptor systems. Time-dependent creep analyses from both macroscopic tensile measurements and microscopic indentation characterizations illustrated that PC$_{71}$BM could effectively immobilize the BHJ interpenetrating networks and alleviate the occurrence of creep deformation. In contrast, BHJ films based on Y6 and PRi-C39 were more prone to creep, and this was more serious in the PRi-C39 system. Contact angle test results demonstrated that the reason for the dissimilar mechanical properties in these films was the different interactions between PM6 and the acceptors. Since the all-polymer system has the lowest elastic modulus, the flexible OPV prepared from the all-polymer active layers is very suitable for the scenario where periodic deformation often takes place. Due to the low fracture strain of the fullerene-based film, the corresponding flexible OPV devices cannot be bent and stretched significantly. It should be noted that, as PC$_{71}$BM based films have the minimum creep deformation, flexible OPV devices using PC$_{71}$BM as acceptor are more suitable for working in a fixed shape for a longer time than

Y6 and PRi-C39 devices. These discussions show that the mechanical properties of the BHJ films are multifaceted. Therefore, this work provides insights into the mechanical properties of the BHJs in PSCs from the macroscale to the microscale, which is beneficial to the materials design and device fabrication of flexible PSCs, thereby promoting the development of flexible PSCs and even flexible electronics.

METHODS

Materials

The electron donor materials PM6, PTB7-Th and D18-Cl and the electron acceptor materials PC$_{71}$BM and Y6 were purchased from Solarmer Materials Inc., Beijing. The polymer acceptor material PRi-C39 was synthesized according to prior literature[18].

Preparation of BHJ films

Glass substrates were firstly cleaned using consecutive ultrasonic baths in acetone, detergent, deionized water, and isopropyl alcohol, respectively, and then dried in an oven. For the FOW samples, substrates were treated with oxygen plasma for 5 min, and then a 40 nm-thick poly(styrene sulfonate)-doped poly(ethylenedioxythiophene) (PEDOT:PSS, Clevios AI 4083) film was obtained by spin-coating on the glass. The substrates were subsequently dried at 150 °C. After that, the mixture solutions of donor and acceptor (1:1.2 w/w, chlorobenzene as the solvent) were spin-casted in an N$_2$-glovebox and baked at 120 °C for 10 min. The thickness of the BHJ films was kept around 100 nm. For the nanoindentation sample preparation, the BHJ films of about 1 μm were directly spin-coated on glass substrates which were treated with plasma for 5 min, then the films were annealed at 120 °C for 10 min.

Characterizations

In the FOW measurements, the BHJ films were cut into a dog-bone shape by laser etching and transferred onto the water surface. The sample was then fixed with the PDMS on the fixture through Van der Walls interaction. The load values were measured by a load cell with high resolution (LTS–10GA, KYOWA, Japan), and the strain values were recorded through a micro mechanical testing system (IBTC–300, CARE, China). During the tensile creep test, the constant stress applied to the sample was 13.25 MPa. The nanoindentation tests (including nano-DMA characterizations) were conducted with a nanoindenter (TI980, Bruker, USA) equipped with a Berkovich diamond indenter with a radius of ≈120 nm. To get the values of h_e, h_p, and h_c, a loading rate of 40 μN s^{-1}, a load of 40 μN that held for 100 s, and an unloading rate of 40 μN s^{-1} were preset. Modulus and hardness profiles were recorded in an automatic measurement mode, in which the loading, holding, and unloading durations were all 0.1 s. The sample preparation conditions of nano-DMA were the same as those of the nanoindentation test. Experiments were performed at room temperature over the frequency range from 25 to 300 Hz. During the test, a small oscillation (1 μN) was superimposed on a constant quasi-static force of 40 μN. The contact angles were estimated with a goniometer equipped with a CCD camera (Model JY–82, China).

DATA AVAILABILITY

The experimental data that support the findings of this study are available from the corresponding author upon reasonable request.

REFERENCES

1. Yang, F., Huang, Y. T., Li, Y. & Li, Y. Large-area flexible organic solar cells. npj Flex. Electron. 5, 30 (2021).
2. Fukuda, K., Yu, K. & Someya, T. The future of flexible organic solar cells. Adv. Energy Mater. 10, 2000765 (2020).
3. Lungenschmied, C. et al. Flexible, long-lived, large-area, organic solar cells. Sol. Energy Mater. Sol. Cells 91, 379–384 (2007).
4. Li, G. et al. High-efficiency solution processable polymer photovoltaic cells by self-organization of polymer blends. Nat. Mater. 4, 864–868 (2005).
5. Cheng, Y.-J., Yang, S.-H. & Hsu, C.-S. Synthesis of conjugated polymers for organic solar cell applications. Chem. Rev. 109, 5868–5923 (2009).
6. Sun, Y. et al. Solution-processed small-molecule solar cells with 6.7% efficiency. Nat. Mater. 11, 44–48 (2012).
7. Zhang, G. et al. Nonfullerene acceptor molecules for bulk heterojunction organic solar cells. Chem. Rev. 118, 3447–3507 (2018).
8. Kim, J.-H. et al. Tensile testing of ultra-thin films on water surface. Nat. Commun. 4, 2520 (2013).
9. Lee, C., Wei, X., Kysar, J. W. & Hone, J. Measurement of the elastic properties and intrinsic strength of monolayer graphene. Science 321, 385–388 (2008).
10. Kim, T. et al. Flexible, highly efficient all-polymer solar cells. Nat. Commun. 6, 8547 (2015).
11. Zhou, K. et al. Unraveling the correlations between mechanical properties, miscibility, and film microstructure in all-polymer photovoltaic cells. Adv. Funct. Mater. 32, 2201781 (2022).
12. Chen, Q. et al. Effects of flexible conjugation-break spacers of non-conjugated polymer acceptors on photovoltaic and mechanical properties of all-polymer solar cells. Nano-Micro Lett. 14, 164 (2022).
13. Oliver, W. C. & Pharr, G. M. Measurement of hardness and elastic modulus by instrumented indentation: advances in understanding and refinements to methodology. J. Mater. Res. 19, 3–20 (2004).
14. Karagiannidis, P. G., Kassavetis, S., Pitsalidis, C. & Logothetidis, S. Thermal annealing effect on the nanomechanical properties and structure of P3HT: PCBM thin films. Thin Solid Films 519, 4105–4109 (2011).
15. Li, H.-C. et al. Nano-scale mechanical properties of polymer/fullerene bulk heterojunction films and their influence on photovoltaic cells. Sol. Energy Mater. Sol. Cells 95, 2976–2980 (2011).
16. Ganesamoorthy, R., Sathiyan, G. & Sakthivel, P. Review: Fullerene based acceptors for efficient bulk heterojunction organic solar cell applications. Sol. Energy Mater. Sol. Cells 161, 102–148 (2017).
17. Yuan, J. et al. Single-junction organic solar cell with over 15% efficiency using fused-ring acceptor with electron-deficient core. Joule 3, 1140–1151 (2019).
18. Jia, T. et al. Synchronously regulating the alkyl side-chain and regioisomer of polymerized small molecule acceptor enabling highly efficient all-polymer solar cells processed with non-halogenated solvent. Chem. Eng. J. 433, 133575 (2022).
19. Zhang, M., Guo, X., Ma, W., Ade, H. & Hou, J. A large-bandgap conjugated polymer for versatile photovoltaic applications with high performance. Adv. Mater. 27, 4655–4660 (2015).
20. Liao, S.-H., Jhuo, H.-J., Cheng, Y.-S. & Chen, S.-A. Fullerene derivative-doped zinc oxide nanofilm as the cathode of inverted polymer solar cells with low-bandgap polymer (PTB7-Th) for high performance. Adv. Mater. 25, 4766–4771 (2013).
21. Qin, J. et al. A chlorinated copolymer donor demonstrates a 18.13% power conversion efficiency. J. Semicond. 42, 010501 (2021).
22. Mun, J. et al. Effect of nonconjugated spacers on mechanical properties of semiconducting polymers for stretchable transistors. Adv. Funct. Mater. 28, 1804222 (2018).
23. Fan, Q. et al. Mechanically robust all-polymer solar cells from narrow band gap acceptors with hetero-bridging atoms. Joule 4, 658–672 (2020).
24. Kim, W. et al. Comparative study of the mechanical properties of all-polymer and fullerene-polymer solar cells: the importance of polymer acceptors for high fracture resistance. Chem. Mater. 30, 2102–2111 (2018).
25. Medvedev, G. A. & Caruthers, J. M. Stochastic model prediction of nonlinear creep in glassy polymers. Polymer 74, 235–253 (2015).
26. Chen, K., Schweizer, K. S., Stamm, R., Lee, E. & Caruthers, J. M. Theory of nonlinear creep in polymer glasses. J. Chem. Phys. 129, 184904 (2008).
27. Lee, H.-N., Riggleman, R. A., de Pablo, J. J. & Ediger, M. D. Deformation-induced mobility in polymer glasses during multistep creep experiments and simulations. Macromolecules 42, 4328–4336 (2009).
28. Yang, J.-L., Zhang, Z., Schlarb, A. K. & Friedrich, K. On the characterization of tensile creep resistance of polyamide 66 nanocomposites. Part II: Modeling and prediction of long-term performance. Polymer 47, 6745–6758 (2006).
29. Yang, S., Zhang, Y. W. & Zeng, K. Analysis of nanoindentation creep for polymeric materials. J. Appl. Phys. 95, 3655–3666 (2004).
30. An, X. et al. Intrinsic mechanical properties of the polymeric semiconductors. J. Mater. Chem. C 8, 11631–11637 (2020).

31. Sreeram, A. et al. Nanomechanical properties of poly (*para*-phenylene vinylene) determined using quasi-static and dynamic nanoindentation. *Polym. Test.* **37**, 86–93 (2014).

32. Zeng, K. *Polymer Tribology* (eds. Sinha, S. K. & Briscoe, B. J.) 141–194 (Imperial College Press, 2009).

33. Danielsen, S. P. O. et al. Molecular characterization of polymer networks. *Chem. Rev.* **121**, 5042–5092 (2021).

34. Díez-Pascual, A. M., Gómez-Fatou, M. A., Ania, F. & Flores, A. Nanoindentation in polymer nanocomposites. *Prog. Mater. Sci.* **67**, 1–94 (2015).

35. Herbert, E. G., Oliver, W. C. & Pharr, G. M. Nanoindentation and the dynamic characterization of viscoelastic solids. *J. Phys. D: Appl. Phys.* **41**, 074021 (2008).

36. Venugopal, G. et al. Nano-dynamic mechanical and thermal responses of single-walled carbon nanotubes reinforced polymer nanocomposite thin films. *J. Alloy. Compd.* **688**, 454–459 (2016).

37. Rajeshwari, P., Rao, V. V. & Dey, T. K. Depth-sensing indentation and nano-dynamic mechanical properties of aluminum nitride nanoparticles reinforced high density poly-ethylene nanocomposites. *Polym. Compos.* **40**, 240–254 (2019).

38. Gao, M., Liang, Z., Geng, Y. & Ye, L. Significance of thermodynamic interaction parameters in guiding the optimization of polymer:nonfullerene solar cells. *Chem. Commun.* **56**, 12463–12478 (2020).

ACKNOWLEDGEMENTS

AUTHOR CONTRIBUTIONS

T.Z. and F.G. contribute equally to this work. B.X. and R.Y. directed this work. T.Z. and F.G. conducted experiments, fabricated devices, and analyzed data. S.L., Q.L. and X.W. helped to analyze the data. T.J. provided the materials. All authors contributed to the manuscript revisions.

COMPETING INTERESTS

The authors declare no competing interests.

ADDITIONAL INFORMATION

Supplementary information The online version contains supplementary material available at https://doi.org/10.1038/s41528-023-00236-5.

Correspondence and requests for materials should be addressed to Biao Xiao, Tao Jia or Renqiang Yang.

Reprints and permission information is available at http://www.nature.com/reprints

Publisher's note Springer Nature remains neutral with regard to jurisdictional claims in published maps and institutional affiliations.